NANOSYSTEMS:
PHYSICS, CHEMISTRY, MATHEMATICS

Original article

Vinogradov V.Yu., et al. *Nanosystems: Phys. Chem. Math.*, 2026, **17** (2), 218–227.
http://nanojournal.ifmo.ru
DOI 10.17586/2220-8054-2026-17-2-218-227

Effect of hydroxide precursor synthesis conditions on the properties of $Gd_2Zr_2O_7$ spark plasma sintered ceramics

Vladimir Yu. Vinogradov[1,a], Dina V. Dudina[2,b], Maksim A. Esikov[2,c], Olga B. Shcherbina[1,d], Vadim V. Efremov[3,e], Alexander M. Kalinkin[1,f]

[1]Tananaev Institute of Chemistry and Technology of Rare Elements and Mineral Raw Materials KSC RAS, Apatity, Russia

[2]Lavrentyev Institute of Hydrodynamics SB RAS, Novosibirsk, Russia

[3]Institute of North Industrial Ecology Problems KSC RAS, Apatity, Russia

[a]v.vinogradov@ksc.ru, [b]ddudina@hydro.nsc.ru, [c]esmax@ya.ru, [d]o.shcherbina@ksc.ru, [e]v.efremov@ksc.ru, [f]a.kalinkin@ksc.ru

Corresponding author: V.Yu. Vinogradov, v.vinogradov@ksc.ru

PACS 81.05.Je, 81.05.Hf, 81.16.Rt, 81.16.Tb, 81.40.Gh

ABSTRACT The paper presents the first comparative study of the microstructure and mechanical properties of gadolinium zirconate ceramics produced by spark plasma sintering of powders obtained using hydroxide precursors synthesized with and without mechanical activation. The initial precursor was prepared via reverse coprecipitation of hydroxides. Mechanical activation of the precursor was performed in an AGO-2 planetary mill at a centrifugal acceleration of 20 g for 30 min. X-ray phase analysis revealed that the resulting ceramics were nanocrystalline. The ceramics produced from the mechanically activated precursor demonstrated superior mechanical properties, including higher microhardness and Young's modulus, compared to those produced from the non-activated precursor.

KEYWORDS gadolinium zirconate, ceramics, mechanical activation, precursor, spark plasma sintering

ACKNOWLEDGEMENTS This research was conducted within the framework of the budget projects FMEZ-2025-0056 for the Tananaev Institute of Chemistry of the Federal Research Centre of Kola Science Centre of the Russian Academy of Sciences.

FOR CITATION Vinogradov V.Yu., Dudina D.V., Esikov M.A., Shcherbina O.B., Efremov V.V., Kalinkin A.M. Effect of hydroxide precursor synthesis conditions on the properties of $Gd_2Zr_2O_7$ spark plasma sintered ceramics. *Nanosystems: Phys. Chem. Math.*, 2026, **17** (2), 218–227.

1. Introduction

REE zirconates are complex oxides in binary systems of the type Ln_2O_3–MO_2 (where Ln represents rare-earth cations and M denotes Group IVB metal cations: Ti, Zr, Hf). These compounds typically adopt the general formula $Ln_2M_2O_7$ and most commonly crystallize in pyrochlore-type structures with varying degrees of disorder. The extent of structural disorder depends on intrinsic factors – such as chemical composition, bonding nature, and the ratio of cationic radii (R_{Ln}/R_{Zr}) – as well as extrinsic factors, including synthesis conditions [1, 2]. In terms of its structural and chemical characteristics, $Gd_2Zr_2O_7$ occupies a special position in the series of REE zirconates. The corresponding ratio of the radii of the REE and zirconium cations ($R_{Gd}/R_{Zr} = 1.462$) actually delimits two regions of stability: at $R_{Ln}/R_{Zr} \geq 1.46$, the pyrochlore structure (space group $Fd\bar{3}m$) is stable, and, at $R_{Ln}/R_{Zr} < 1.46$, the disordered fluorite structure (space group $Fm\bar{3}m$) becomes favorable [1, 3, 4]. At room temperature, $Gd_2Zr_2O_7$ typically adopts the stable pyrochlore phase (P-$Gd_2Zr_2O_7$), which transforms into a disordered fluorite modification (F-$Gd_2Zr_2O_7$) at ∼1550 °C. As the energy difference between these phases is small, fluorite-like $Gd_2Zr_2O_7$ can exist under standard conditions, which is facilitated by certain conditions of its synthesis [5, 6]. In this regard, REE zirconates, in particular $Gd_2Zr_2O_7$, are interesting from the point of view of the occurrence of a phase transition of the pyrochlore (order) – fluorite (disorder) type [1, 2].

At the same time, REE zirconates with both crystal structures exhibit a broad spectrum of physical and chemical properties, making them highly attractive for fundamental and applied research [7–10]. Their unique structural features and exceptional characteristics render them promising candidates for applications in electro/photocatalysis, magnetism, nuclear waste storage, thermal barrier coatings, sensors, catalysis, ionic conductors, oxygen monitoring, photoluminescent host materials, and solid electrolytes in high-temperature fuel cells [11–21]. In particular, $Gd_2Zr_2O_7$ demonstrates high thermal stability, chemical resistance, high thermal expansion coefficient ($11.09 \cdot 10^{-6}$ K^{-1} [22]), a high melting point

(2570 °C) [23], low thermal conductivity (1.5 – 2.0 W/(m·K) [5, 24]), and high ionic conductivity ($> 1 \cdot 10^{-3}$ Sm/cm at 800 °C [25, 26]).

In recent years, researchers have increasingly focused on enhancing the synthesis methods for nanoceramics based on REE zirconates. These materials exhibit superior properties compared to microcrystalline ceramics, including higher radiation resistance, lower thermal conductivity, and enhanced oxygen-ion conductivity [1, 4, 14, 27–36].

The properties and applicability of ceramics based on rare earth zirconates are directly influenced by the composition, size, shape, and morphology of their precursors, which can be synthesized through various methods [1, 4, 14, 37, 38]. Typically, precursors for rare earth zirconate nanoceramics – including $Gd_2Zr_2O_7$ – are prepared using wet chemistry techniques such as sol-gel synthesis, solvothermal, hydrothermal methods, and hydroxide coprecipitation [6, 11, 14, 30, 31, 39–41].

Another crucial step in ceramic production is selecting the consolidation method. Spark plasma sintering (SPS) has emerged as a promising technique for compacting and consolidating various materials. During SPS, an electric current passes through the tooling and the sample, rapidly heating them via the Joule effect. This allows the target processing temperature to be achieved in minimal time. Additionally, the applied pressure significantly enhances densification. Thus, SPS can consolidate powder system components at lower temperatures while suppressing excessive grain growth [42–44]. The key advantages of SPS technology include:

- High densification with controllable porosity.
- Elimination of pre-compaction or binders, simplifying the process.
- Homogeneous sintering of both similar and dissimilar materials.
- Rapid processing due to short cycle times.
- Minimal grain growth, preserving the microstructure [45, 46].

In this work, nanocrystalline $Gd_2Zr_2O_7$ ceramics were synthesized by SPS using a dried powder of hydroxide precursor prepared through the coprecipitation of gadolinium and zirconium hydroxides. For the first time, the influence of preliminary mechanical activation (MA) of the hydroxide precursor on the mechanical properties of the ceramics – specifically, microhardness and Young's modulus – was investigated.

2. Experimental

For the synthesis of the initial and MA-precursors of gadolinium zirconate, "chemically pure" gadolinium nitrate $Gd(NO_3)_3 \cdot 6H_2O$ ($\omega(Gd_2O_3)$ = 40.48 %), zirconium oxychloride $ZrOCl_2 \cdot 8H_2O$ ($\omega(ZrO_2)$ = 37.98 %) and ammonium hydroxide NH_4OH were used. The detailed synthesis method for the hydroxide precursor is described in the previously published work [47]. After obtaining the precursor, it was dried at 110 °C for 12 hours. This precursor is hereafter referred to as the initial precursor (IP).

The IP was subjected to mechanical activation. MA was performed in an AGO-2 centrifugal–planetary mill under ambient conditions. The process utilized zirconium dioxide–lined vials and 7 – 8 mm zirconium dioxide grinding balls [47]. The milling parameters were as follows: centrifugal acceleration – 20 g, duration – 30 min, and a ball-to-powder mass ratio of 20:1. To ensure homogeneity, the mill was paused every 60 seconds, and the contents were manually mixed using a spatula. The resulting mechanically activated precursor is hereafter denoted as MP. The IP and MP were not subjected to additional heat treatment before SPS.

SPS was performed on a SPS Labox 1575 apparatus (SINTER LAND Inc., Japan) using graphite tooling at temperatures of 1300 and 1550 °C (measured by a pyrometer focused on a hole in the wall of the die). The heating rate was ∼60 °/min, the applied pressure was 40 MPa. The samples were held for 5 min at the maximum temperature. Tablets with a diameter of 10 mm and a thickness of 2.0 – 2.5 mm were prepared from powders derived from IP and MP. After SPS, the samples were polished with sandpaper and ultrasonically cleaned in distilled water and alcohol to remove residual graphite from the surface [44]. To completely remove graphite, the tablets were calcined at 1000 °C for 3 hours.

For X-ray diffraction analysis (XRD), a Rigaku Miniflex-600 diffractometer (CuKα radiation) was used. XRD patterns were recorded at a rate of $2^\circ(2\theta)$ per min. The cubic Fm3m structure of gadolinium zirconate $Gd_2Zr_2O_7$ was reliably identified in the diffraction patterns of the samples (PDF No. 04-006-1657). Full-profile analysis of the diffraction patterns using the Rietveld method was performed using SmartLab Studio II software, included with the MiniFlex-600 diffractometer. All reflections were used for the calculation. The initial structural model for the calculations was based on PDF card No. 04-006-1657, which closely matched the observed experimental profile. Angular correction (2θ correction) was performed using the external standard method, with silicon (NIST SRM 640) as the reference material. During full-profile analysis, the background, scale factor, and lattice parameters were refined using the initial parameters provided by the model. The peak profiles were fitted using a pseudo-Voigt function. Structural parameters – including atomic coordinates, site occupancies, and thermal displacement factors – were not refined. The refinement procedure was carried out sequentially as follows: background determination, refinement of the scale factor and lattice parameters, and finally, refinement of the profile function parameters.

The effective crystallite sizes for ceramics and the microstrains were calculated from the XRD data using Size-Microstrain (SSP) graphical method [48, 49]. In order to account for instrumental broadening, a Si (NIST SRM 640f) reference sample was used.

IR spectra were recorded on a Nicolet 6700 FT–IR Fourier spectrometer in KBr tablets.

The mechanical properties of $Gd_2Zr_2O_7$ ceramic samples prepared by SPS with and without preliminary MA of the IP were studied by the contact method using a NanoSkan probe microscope-nanohardness tester (FSBI TISNCM, Russia).

The microstructure of the $Gd_2Zr_2O_7$ ceramic samples obtained from IP and MP was analyzed by scanning electron microscopy (SEM) using a SEM LEO-1450 microscope. The images were processed by Scan Master program.

The density of the synthesized $Gd_2Zr_2O_7$ ceramics was determined using Archimedes' method. Prior to density measurements, all samples were annealed at 1000 °C for 3 hours to ensure the complete removal of residual graphite.

3. Results and discussion

Previous studies [47] demonstrated that both IP and MP, when heat-treated at 900 – 1200 °C, form disordered metastable fluorite-like $Gd_2Zr_2O_7$. The effective crystallite size increases with the calcination temperature, ranging from 10 to 48 nm for IP and from 17 to 56 nm for MP. Notably, the use of MA enables the synthesis of highly dispersed $Gd_2Zr_2O_7$ powders with a specific surface area 5 – 7 times greater than that of powders produced without MA. This enhancement can be attributed to the improved homogeneity of MP and more uniform $Gd_2Zr_2O_7$ crystallization during calcination [47].

Figure 1 presents the XRD patterns of the synthesized ceramics. All ceramic samples exhibit a disordered fluorite structure (PDF No. 04-006-1657) and are nanocrystalline in nature. The effective crystallite sizes for ceramics obtained by SPS IP and MP, as well as the microstrains and lattice parameters are given in Table 1. There was no significant deviation in the crystal lattice parameters of the ceramics produced by SPS IP and MP relative to the theoretical value (PDF No. 04-006-1657, Fd3m, $a = b = c = 5.25$ Å). This indicates that the chemical composition of the produced ceramics is close to $Gd_2Zr_2O_7$ (Gd:Zr mole ratio of 1:1). As an example, Fig. 2 presents experimental (black dots), calculated (red curve) and difference (blue curve) XRD patterns of $Gd_2Zr_2O_7$ ceramics synthesized by SPS at 1300 from MP. The small difference between the calculated and experimental XRD patterns confirms the formation of ceramics with the $Gd_2Zr_2O_7$ structure. To confirm the nanocrystalline structure of the obtained ceramics, further studies using transmission electron microscopy (TEM) are required.

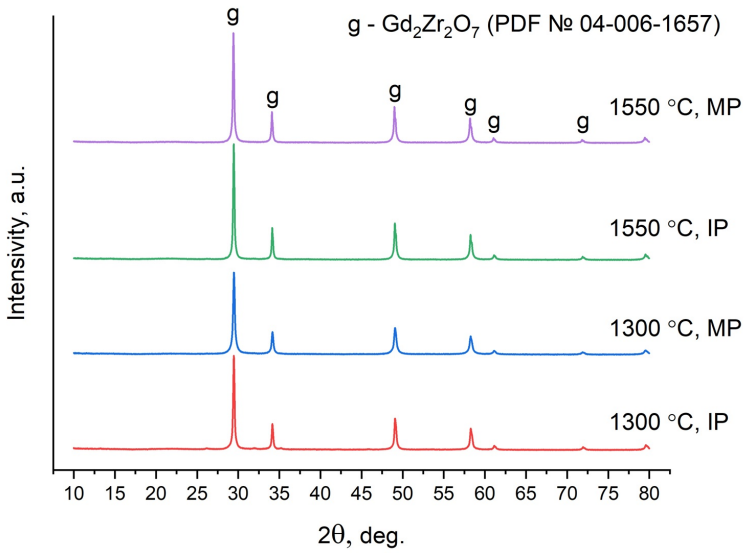

FIG. 1. XRD patterns of $Gd_2Zr_2O_7$ ceramics synthesized by SPS at 1300 and 1550 °C from IP and MP

As mentioned earlier, P-$Gd_2Zr_2O_7$ transforms into F-$Gd_2Zr_2O_7$ at approximately 1550 °C. However, depending on the synthesis method, the fluorite modification can be retained upon cooling. In such cases, an ordered pyrochlore phase may form within the fluorite phase as nanodomains, and the corresponding peaks are not detectable in the XRD patterns. According to the literature [50, 51], infrared spectroscopy is a highly sensitive method for identifying P-$Gd_2Zr_2O_7$ nanodomains within a F-$Gd_2Zr_2O_7$ matrix. The FTIR spectra of the ceramics studied here (Fig. 3) lack the characteristic pyrochlore absorption band at 510 cm^{-1}, which is associated with the $Gd_2Zr_2O_7$ pyrochlore lattice. This absence indicates that P-$Gd_2Zr_2O_7$ nanodomains are not present and that no fluorite-to-pyrochlore structural transition has occurred.

The microhardness (H, GPa) of $Gd_2Zr_2O_7$ ceramics was determined using the comparative sclerometry method, in which scratches are alternately applied to the test material and a reference standard of the known hardness [52]. A certified

TABLE 1. Lattice parameters, crystallite sizes and microstrains of $Gd_2Zr_2O_7$ ceramics

Sample	SPS temperature, °C	Lattice parameter, Å	Crystallite size, nm	Microstrain, %
IP	1300	5.2454	70±6	0.07±0.01
MP	1300	5.2519	64±5	0.07±0.01
IP	1550	5.2595	103±8	0.05±0.01
MP	1550	5.2457	123±10	0.03±0.01

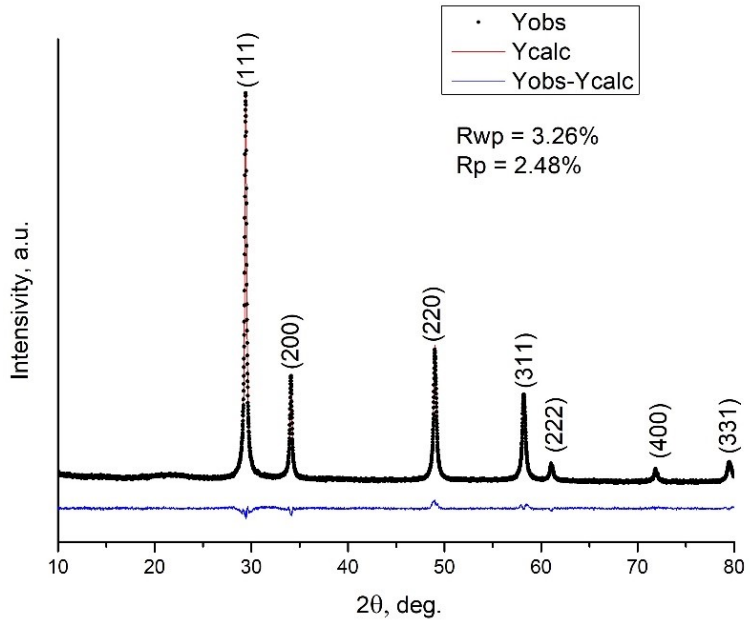

FIG. 2. Single-phase Rietveld refined XRD pattern of $Gd_2Zr_2O_7$ ceramics synthesized by SPS at 1300 °C from MP

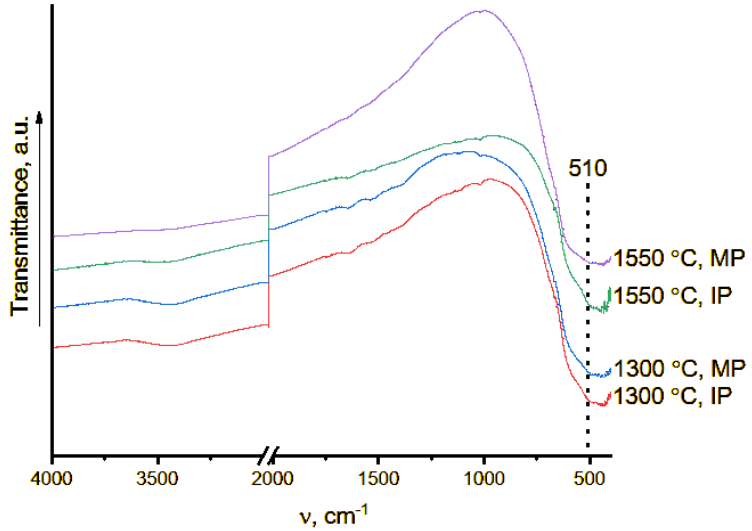

FIG. 3. FTIR spectra of $Gd_2Zr_2O_7$ ceramics synthesized by SPS at 1300 and 1550 °C from IP and MP

fused quartz sample calibrated against the State Hardness Standard (SHS 31-2006) at the Federal State Unitary Enterprise "Russian Metrological Institute of Technical Physics and Radio Engineering" (FSUE "VNIIFTRI") served as the hardness reference. Scratching of $Gd_2Zr_2O_7$ ceramics was performed at indenter loads of 5 – 20 mN using a Berkovich indenter – a triangular diamond pyramid probe with a tip curvature radius of ∼50 nm. The same probe was used to scan the scratched surface. As an example, Fig. 4 shows the resulting scratch topography of the ceramics prepared from IP and MP by SPS at 1300 °C.

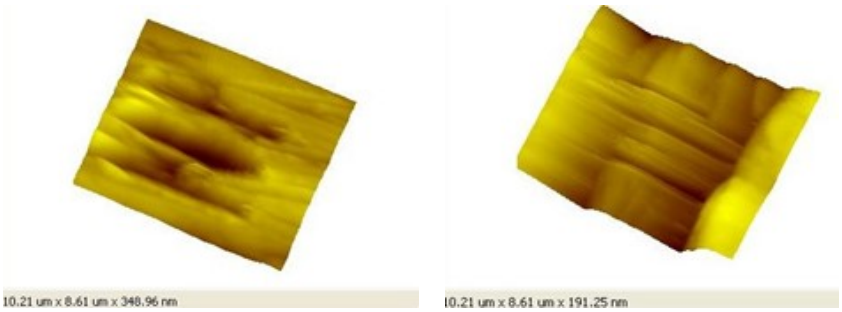

(a) (b)

FIG. 4. Surface morphology of $Gd_2Zr_2O_7$ ceramics prepared from IP (a) and MP (b) by SPS at 1300 °C after sclerometry

Since the forward motion of a Berkovich indenter at an acute angle during scratching resembles the extrusion of an imprint in a Vickers test, the calculations were based on a model for Vickers pyramid indentation [52–54]. The hardness of the material was determined using the following formula:

$$H = k \cdot \frac{P}{b^2}, \tag{1}$$

where P is the normal force with which the scratch was made, expressed in Newtons; b is the arithmetic mean of the scratch width, expressed in meters and k is the indenter shape factor for a given scratch width. The indenter shape factor k was determined by scratching a reference material with the known hardness and calculating it using the following formula:

$$k = \frac{H_c \cdot b^2}{P}, \tag{2}$$

where H_c is the hardness of the reference material.

To measure the absolute value of Young's modulus (E, GPa) of ceramics, force spectroscopy was employed [53–55]. This technique involves bringing an oscillating indenter into contact with the sample surface, where it vibrates normal to the surface with an amplitude of less than 10 nm and a frequency of ∼12 kHz. A triangular diamond pyramid with an apex angle of approximately 60° was used as the indenter needle featuring a tip curvature radius of ∼100 nm. The needle's Young's modulus (E) and Poisson's ratio (ν) were set to 1140 GPa and 0.07, respectively, in the calculations. As the indenter interacts with the material, the frequency of the probe oscillations increases upon contact with the surface. According to the Hertz model, the slope of the oscillation frequency versus penetration depth (approach curve) is proportional to the elastic modulus of the material [53, 54]. The elastic modulus was determined by comparing the slopes of the approach curves for the sample and a reference material. For each sample, the Young's modulus values were calculated as the average of 16 independent measurements.

The relative density of all prepared ceramics exceeds 90 %, reaching near-theoretical values [1] after SPS at 1550 °C (Table 2).

The data in Table 2 demonstrate that MA of the precursor enhances the mechanical properties of the gadolinium zirconate ceramics. For both SPS temperatures (1300 and 1550 °C), the microhardness and Young's modulus values of ceramics derived from the MP are significantly higher than those of ceramics produced from IP. For comparison, Table 2 presents the literature data on the properties of $Gd_2Zr_2O_7$ ceramics with a fluorite structure prepared via SPS [56] and conventional solid-phase free sintering [57, 58]. When consolidated by SPS, our precursor (MP) demonstrates advantages over the gel-drying and combustion-derived precursor, yielding ceramics with higher microhardness and density. The solid-phase method enables the production of ceramics with microhardness and Young's modulus values close to those obtained in our work. However, this method requires prolonged high-temperature calcination, which hinders the synthesis of nanocrystalline samples (Table 2).

The trends in the microhardness and Young's modulus for ceramics obtained by SPS of IP and MP can be explained as follows.

Young's modulus (elastic modulus) is a fundamental characteristic of a material, a measure of the interatomic bonding forces. It describes elastic deformation, which is reversible. In ceramics, pores are the primary factor weakening the elastic

TABLE 2. Relative density ($\rho_{\text{rel.}}$), microhardness (*HV*) and Young's modulus (E) of F-$Gd_2Zr_2O_7$ ceramics prepared by different methods

Precursor	Consolidation	$\rho_{\text{rel.}}$, %	*HV*, GPa	E, GPa	Ref.
IP	SPS: 1300 °C, 40 MPa, 5	95.9	6.2±1.3	205±3	This work
MP	SPS: 1300 °C, 40 MPa, 5	91.3	15.3±2.3	261±9	This work
IP	SPS: 1550 °C, 40 MPa, 5	98.9	8.2±1.4	272±3	This work
MP	SPS: 1550 °C, 40 MPa, 5	99.0	9.2±1.1	298±11	This work
Drying and combustion of gel	SPS: 1300 °C, 70 MPa, 5 min	97.4	8.8±0.4	—	[56]
Mixture of oxides	Solid-phase method: 1600 °C, 10 h	98.4	10.9±0.9	307±31	[57]
Mixture of oxides	Solid-phase method: 1650 °C, 10 h	99.0	6.0±0.3	214±5	[58]

modulus. They concentrate stress and do not contribute to the elastic stiffness of the material. As the sintering temperature increases, porosity decreases, the material becomes denser, and Young's modulus increases. As follows from Table 2, this trend is observed for IP and MP.

Microhardness is sensitive to (1) defects (porosity, cracks) and (2) grain size. When the sintering temperature increases, coalescence and grain growth occur. Fine grains create more boundaries, which act as obstacles to the movement of dislocations and the development of plastic deformation under the indenter. Large grains facilitate this movement, reducing microhardness. On the other hand, an increase in temperature is generally accompanied by an increase in density and the contact area between particles, leading to an increase in hardness. For IP, as the temperature increases, the hardness increases, which likely indicates the predominant influence of the first factor (density/contact area). In the case of MP, the situation is opposite, i.e., grain growth apparently plays the determining role.

Another notable feature of the data presented in Table 2 is that the relative density of the ceramics obtained at 1300 °C from the MP is lower than that of ceramics from the IP. Interestingly, despite this lower density, the microhardness of the ceramics prepared from MP is the highest. It was previously established that both hydroxide precursors (IP and MP) interact with atmospheric carbon dioxide during synthesis, leading to the formation of carbonate groups. In the case of MP, the decomposition of these carbonate groups with the release of CO_2 occurs at higher temperatures compared to IP [47]. We assume that this may be the reason for the reduced density of the MP-based ceramics sintered at 1300 °C. SPS is characterized by very rapid heating (within a few minutes) with simultaneous pressure application. Sintering is accompanied by the removal of volatile components – such as water and CO_2 – from the particle surfaces and from the pores within the sample under highly nonequilibrium conditions.

When the precursor is compacted, the closure of pores is inhibited by the pressure of gases trapped within them. As the removal of carbon dioxide from the MP is more difficult than from the IP, this can lead to a higher degree of closed porosity. However, when the SPS temperature is increased to 1550 °C, the negative factors that limit densification at 1300 °C are overcome. As a result, both the IP and MP achieve high and nearly equal relative densities (98.9 % and 99.0 %, respectively, as shown in Table 2). It is likely that the sample with a density of 91.3 % and maximum microhardness was sintered under optimal conditions for suppressing grain growth. A higher density (98 – 99 %) is achieved by increasing the sintering temperature, which inevitably leads to coalescence and grain growth. As previously noted, larger grains reduce hardness, while smaller grains create more grain boundaries. These boundaries act as obstacles to dislocation movement and hinder the development of plastic deformation beneath the indenter. A detailed clarification of the reasons for the different influence of sintering temperature on the microhardness of ceramics based on IP and MP requires additional research.

The microstructure of $Gd_2Zr_2O_7$ ceramic samples prepared by the SPS method with and without preliminary MA of the IP was analyzed using SEM imaging. The images were processed using Scan Master program, designed for the mathematical analysis of such micrographs. The program enables users to select objects within an image, analyze their characteristics, and perform the statistical processing on the set of selected objects based on the chosen criteria. In this case, parameter "Length" – defined as the maximum length among 18 projections of an object onto a plane – was selected as the criterion for evaluating the size of the ceramic particles.

SEM images of the $Gd_2Zr_2O_7$ ceramic material synthesized by SPS at 1300 °C using IP reveal a nearly pore-free surface with no discernible grains (Fig. 5). SEM images of the $Gd_2Zr_2O_7$ ceramic material synthesized by SPS at 1300 °C using MP is shown in Fig. 6.

Increasing the SPS temperature to 1550 °C results in grain growth. The $Gd_2Zr_2O_7$ ceramics synthesized from the IP at this temperature exhibit well-faceted grains ranging from 0.2 to 3.0 μm in size (Fig. 7), with an average grain size of 0.4 μm (Fig. 8). Microcracks are observed along the grain boundaries, but the ceramics are nearly pore-free.

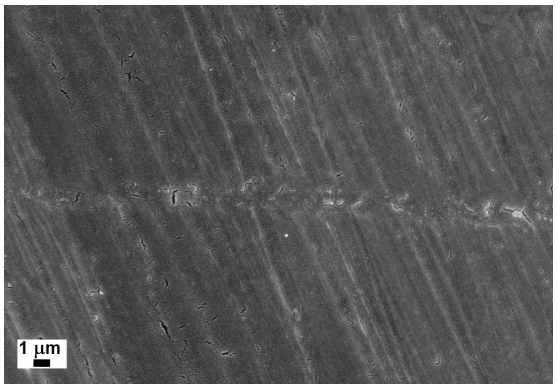

FIG. 5. SEM image of $Gd_2Zr_2O_7$ ceramic material prepared by the SPS at 1300 °C from IP (magnification 5000)

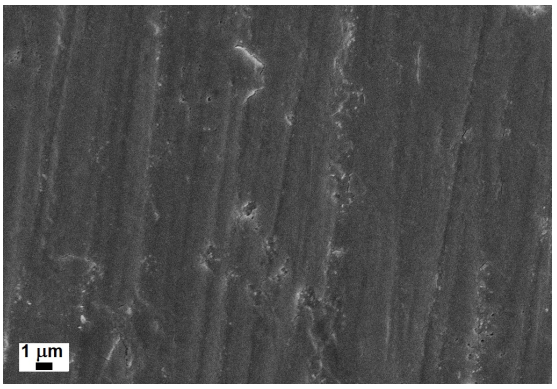

FIG. 6. SEM image of $Gd_2Zr_2O_7$ ceramic material prepared by the SPS at 1300 °C from MP (magnification 5000)

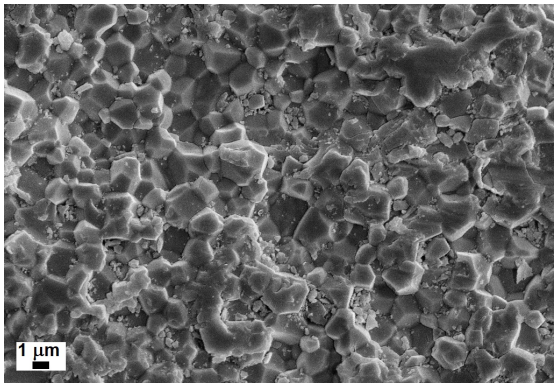

FIG. 7. SEM image of $Gd_2Zr_2O_7$ ceramic material prepared by SPS at 1550 °C from IP (magnification 5000)

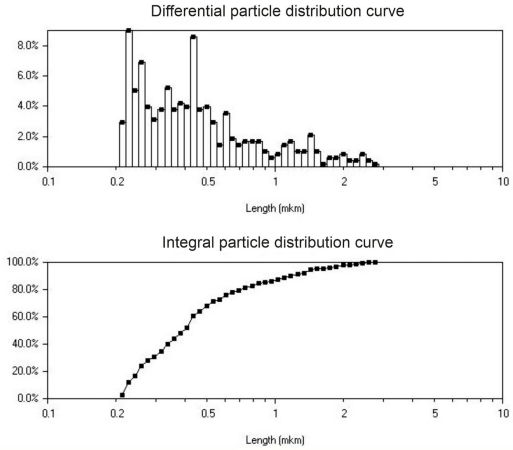

FIG. 8. Differential curve of grain distribution and integral curve of granulometric composition of $Gd_2Zr_2O_7$ ceramic material prepared by SPS at 1550 °C from IP

The $Gd_2Zr_2O_7$ ceramic samples prepared from MP at 1550 °C exhibit at least two distinct morphological structures (Fig. 9). These include regions composed of well-defined, faceted grains ranging from 0.1 to 1.5 μm in size and larger areas (up to 8 – 10 μm in length) lacking a pronounced grain structure (Figs. 9 and 10).

The SEM image of the $Gd_2Zr_2O_7$ ceramic material synthesized by SPS at 1550 °C (IP, higher magnification, Fig. 11) confirms a non-porous surface. The microstructure exhibits the features of brittle fracture, including a crystalline structure and intergranular cleavage facets. In contrast, the MP-based sample at the same magnification (Fig. 12) shows pronounced grain agglomeration. The intergranular boundaries are nearly invisible in the image, with the grains in close contact. The surface of this sample is smoother and exhibits fewer visible defects compared to the IP-based sample (Fig. 11). Cleavage predominantly occurs along intergranular contacts, while intragranular chips are extremely rare.

4. Conclusions

Nanocrystalline $Gd_2Zr_2O_7$ ceramics were synthesized by SPS using the hydroxide precursor with and without MA. The relative density of all the prepared ceramics is greater than 90 %. This value approaches the theoretical value after SPS at 1550 °C. MA of the initial precursor led to an increase in the microhardness and Young's modulus of the sintered ceramics. So, the highest values were achieved for the ceramics derived from the MP: a microhardness of 15.3±2.3 GPa (at 1300 °C) and a Young's modulus of 298±11 GPa (at 1550 °C). The comparison of the obtained results with the literature data on F-$Gd_2Zr_2O_7$ SPS-ceramics revealed that our MP precursor exhibits a higher efficiency in enhancing the microhardness of the ceramics compared to the precursor derived from gel drying and combustion. While conventional solid-phase synthesis of F-$Gd_2Zr_2O_7$ ceramics yields microhardness and Young's modulus values similar to our findings, this method requires prolonged high-temperature calcination, which prevents the formation of nanocrystalline materials. Although the crystallite size has a minimal direct impact on microhardness and Young's modulus, its control

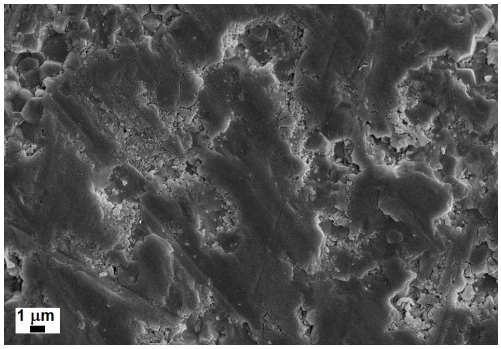

FIG. 9. SEM image of $Gd_2Zr_2O_7$ ceramic material prepared by SPS at 1550 °C from MP (magnification 5000)

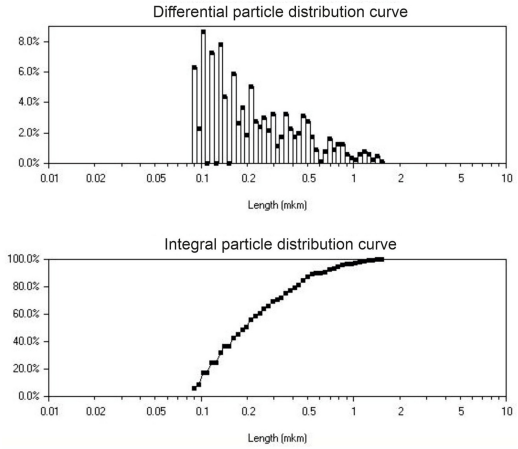

FIG. 10. Differential curve of grain distribution and integral curve of granulometric composition of $Gd_2Zr_2O_7$ ceramic material prepared by SPS at 1550 °C from MP

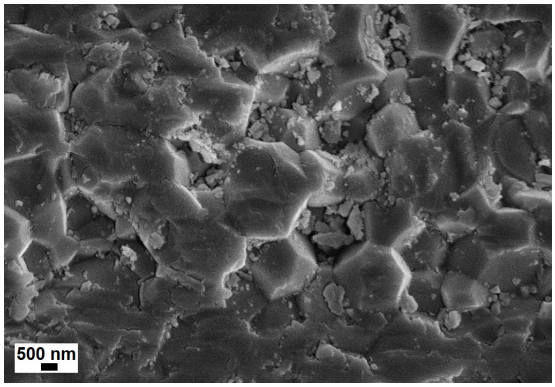

FIG. 11. SEM image of $Gd_2Zr_2O_7$ ceramic material prepared by SPS at 1550 °C from IP (magnification 10000)

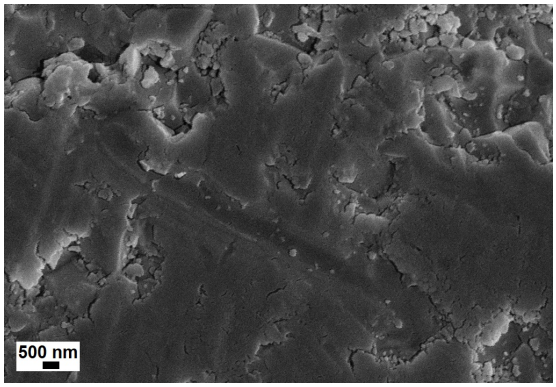

FIG. 12. SEM image of $Gd_2Zr_2O_7$ ceramic material prepared by SPS at 1550 °C from MP (magnification 10000)

remains crucial for practical applications. For instance, in functional materials like thermal barrier coatings, the production of nanocrystalline ceramics is highly important. This is because key physicochemical properties – such as thermal conductivity and heat capacity – are directly influenced by the crystallite size of the resulting ceramic material.

References

[1] Subramanian M., Aravamudan G., Subba Rao G.V. Oxide Pyrochlores – a Review. *Prog. Solid State Chem*., 1983, **15** (2), P. 55–143.

[2] Pokhrel M., Alcoutlabi M., Mao Yu. Optical and X-ray Induced Luminescence from Eu^{3+} Doped $La_2Zr_2O_7$ Nanoparticles. *J. Alloy. Compd.*, 2017, **693**, P. 719–729.

[3] Zhang J., Guo X., Jung Ye.–G., Li L., Knapp J. Lanthanum Zirconate Based Thermal Barrier Coatings: A Review. *Surf. Coat. Technol*., 2017, **323**, P. 1–12.

[4] Teymourinia H. Advanced Rare Earth–Based Ceramic Nanomaterials. Chapter 4 – Rare Earth Zirconate ($Re_2Zr_2O_7$) Ceramic Nanomaterials. *Elsevier Series on Advanced Ceramic Materials*, 2022, P. 77–103.

[5] Diaz-Guillen J.A., Dura O.J., Diaz-Guillen M.R., Bauer E., Lopez de la Torre M.A., Fuentes A.F. Thermophysical Properties of $Gd_2Zr_2O_7$ Powders Prepared by Mechanical Milling: Effect of Homovalent Gd^{3+} Substitution. *J. Alloys Compd.*, 2015, **649**, P. 1145–1150.

[6] Popov V.V., Menushenkov A.P., Yaroslavtsev A.A., Kulik E.S., Petrunin V.F., Korovin S.A., Zubavichus Ya.V., Trofmova N.N. Short and Long-Range Order Balance in Nanocrystalline $Gd_2Zr_2O_7$ Powders with a Fluorite-Pyrochlore Structure. *Russ. J. Inorg. Chem.*, 2014, **59**, P. 279–285.

[7] Fuentes A.F., Montemayor S.M., Maczka M., Lang M., Ewing R.C., Amador U. A Critical Review of Existing Criteria for the Prediction of Pyrochlore Formation and Stability. *Inorg. Chem*., 2018, **57** (19), P. 12093–12105.

[8] Vassen R., Jarligo M.O., Steinke T., Mack D.E., Stöver D. Overview on Advanced Thermal Barrier Coatings. *Surf. Coat. Technol*., 2010, **205**, P. 938–942.

[9] Feng J., Xiao B., Wan C. L., Qu Z. X., Huang Z. C., Chen J. C., Zhou R., Pan W. Electronic Structure, Mechanical Properties and Thermal Conductivity of Ln(2)Zr(2)O(7) (Ln = La, Pr, Nd, Sm, Eu and Gd) Pyrochlore. *Acta Mater*., 2011, **59**, P. 1742–1760.

[10] Lang M., Zhang F., Zhang J., Wang J., Lian J., Weber W.J., Schuster B., Trautmann C., Neumann R., Ewing R.C. Review of A(2)B(2)O(7) Pyrochlore Response to Irradiation and Pressure. *Nucl. Instrum. Methods Phys. Res., Sect. B*., 2010, **268**, P. 2951–2959.

[11] Duarte W., Vardelle M., Rossignol S. Effect of the Precursor Nature and Preparation Mode on the Coarsening of $La_2Zr_2O_7$ Compounds. *Ceram. Int*., 2016, **42**, P. 1197–1209.
[12] Xu C., Wang L., Bai B., Peng L., Cai S. Rapid Synthesis of $Gd_2Zr_2O_7$ Ceramics by Flash Sintering and Its Aqueous Durability. *J. Eur. Ceram. Soc*., 2020, **40**, P. 1620–1625.
[13] Sivakumar S., Praveen K., Shanmugavelayutham G. Preparation and Thermophysical Properties of Plasma Sprayed Lanthanum Zirconate. *Mater. Chem. Phys*., 2018, **204**, P. 67–71.
[14] Zinatloo-Ajabshir S., Salavati-Niasari M., Sobhari A., Zinatloo-Ajabshir Z. Rare Earth Zirconate Nanostructures: Recent Development on Preparation and Photocatalytic Applications. *J. Alloys Compd*., 2018, **767**, P. 1164–1185.
[15] Ewing R.C., Weber W.J., Lian J. Nuclear Waste Disposal-Pyrochlore ($A_2B_2O_7$): Nuclear Waste Form for the Immobilization of Plutonium and "Minor" Actinides. *J. Appl. Phys*., 2004, **95**, P. 5949–5971.
[16] Zhou D., Mack D.E., Bakan E., Mauer G., Sebold D., Guillon O., Vaßen R. Thermal Cycling Performances of Multilayered Yttria–stabilized Zirconia/Gadolinium Zirconate Thermal Barrier Coatings. *J. Am. Ceram. Soc*., 2020, **103**, P. 2048–2061.
[17] Brykała U., Diduszko R., Jach K., Jagielski, J. Hot pressing of gadolinium zirconate pyrochlore. *Ceram. Int*., 2015, **41**, P. 2015–2021.
[18] Liu Z.G., Ouyang J.H., Zhou Y., Xia X.L. Electrical Conductivity of Defect Fluorite-Type $(Gd_{1-x}Yb_x)_2Zr_2O_7$ Solid Solutions. *J. Alloys Compd*., 2010, **490**, P. 277–281.
[19] Srinivasulu K., Manisha Vidyavathy S. Effect of Different Calcination Techniques on the Morphology and Powder Flowability Characteristics of Rare-Earth Zirconates ($Re_2Zr_2O_7$; Re=La, Gd, Nd, Y) Synthesized by Solid-State High-Energy Milling Process. *J. Ceramic. Process. Res*., 2019, **20**, P. 8–17.
[20] Keyvani A., Mahmoudinezhad P., Jahangiri A., Bahamirian M. Synthesis and Characterization of $((La_{1-x}Gd_x)_2Zr_2O_7$; $x = 0, 0.1, 0.2, 0.3, 0.4, 0.5, 1)$ Nanoparticles for Advanced TBCs. *J. Aust. Ceram. Soc*., 2020, **56**, P. 1543–1550.
[21] Lei M., Weimin M., Xudong S., Jianan L., Lianyong J., Han S. Structure Properties and Sintering Densification of $Gd_2Zr_2O_7$ Nanoparticles Prepared via Different Acid Combustion Methods. *J. Rare Earths*, 2015, **33**, P. 195–201.
[22] Wang C., Guo L., Zhang Y., Zhao X., Ye F. Enhanced Thermal Expansion and Fracture Toughness of Sc_2O_3-doped $Gd_2Zr_2O_7$ Ceramics. *Ceram. Int*., 2015, **41**, P. 10730–10735.
[23] Karaulov A.G., Zoz E.I., Shlyakhova T.M. Structure and Properties of Refractories Based on Zirconia Stabilized by Gadolinium Oxide. *Refract. Ind. Ceram*., 1996, **37**, P. 83–87.
[24] Pan W., Phillpot S.R., Wan C.L., Chernatynskiy A., Qu Z.X. Low Thermal Conductivity Oxides. *Mater. Res. Bull*., 2012, **37**, P. 917–922.
[25] Diaz-Guillen J.A., Fuentes A.F., Diaz-Guillen M.R., Almanza J.M., Santamaria J., Leon C. The Effect of Homovalent A-site Substitutions on the Ionic Conductivity of Pyrochlore-type $Gd_2Zr_2O_7$. *J. Power. Sources*., 2009, **186**, P. 349–352.
[26] Cao X.Q., Vassen R., Stöver D. Ceramic Materials for Thermal Barrier Coatings. *J. Eur. Ceram. Soc*., 2004, **24** (1), P. 1–10.
[27] Torres-Rodriguez J., Gutierrez-Cano V., Menelaou M., Kaštyl J., Cihlář J., Tkachenko S., González J.A., Kalmár J., Fábián I., Lázár I., Čelko L., Kaiser J. Rare-Earth Zirconate $Ln_2Zr_2O_7$ (Ln: La, Nd, Gd, and Dy) Powders, Xerogels, and Aerogels: Preparation, Structure, and Properties. *J. Inorg. Chem.*, 2019, **58** (21), P. 14467–14477.
[28] Kong S.L., Karatchevtseva I., Gregg D.J., Blackford M.G., Holmes, R., Triani, G. $Gd_2Zr_2O_7$ and $Nd_2Zr_2O_7$ Pyrochlore Prepared by Aqueous Chemical Synthesis. *J. Eur. Ceram. Soc*., 2013, **33**, P. 3273–3285.
[29] Kaliyaperumal C., Sankarakumar A., Paramasivam T. Grain Size Effect on the Electrical Properties of Nanocrystalline $Gd_2Zr_2O_7$ Ceramics. *J. Alloys Compd*., 2020, **813**, 152221.
[30] Li W., Zhang K., Xie D., Deng T., Luo B., Zhang H., Huang X. Characterizations of Vacuum Sintered $Gd_2Zr_2O_7$ Transparent Ceramics Using Combustion Synthesized Nanopowder. *J. Eur. Ceram. Soc*., 2020, **40**, P. 1665–1670.
[31] Yang Y., Huang Z., Shi C., Duan J., Cheng G., Wang H., Wu D., Qi J., Lu T. Liquid-Solid-Solution Synthesis of Ultrafine $Gd_2Zr_2O_7$ Nanoparticles with Yield Enhancement. *Ceram. Int*., 2020, **46**, P. 1216–1219.
[32] Yan C.-H., Yan Z.-G., Du Ya-P., Shen J., Zhang C., Feng W. Controlled Synthesis and Properties of Rare Earth Nanomaterials. *Handbook on the Physics and Chemistry of Rare Earths*, 2011, **41**, P. 275–472.
[33] Zinatloo-Ajabshir S., Niasari-Salavati M., Zinatloo-Ajabshir Z. $Nd_2Zr_2O_7$–Nd_2O_3 Nanocomposites: New Facile Synthesis, Characterization and Investigation of Photocatalytic Behaviour. *Mater. Lett*., 2016, **180**, P. 27–30.
[34] Zinatloo-Ajabshir S., Niasari-Salavati M., Zinatloo-Ajabshir Z. Facile Size–Controlled Preparation of Highly Photocatalytically Active Praseodymium Zirconate Nanostructures for Degradation and Removal of Organic Pollutants. *Sep. Pur. Technol*., 2017, **177**, P. 110–120.
[35] Sytschev A.E., Merzhanov A.G. Self-propagating high-temperature synthesis of nanomaterials. *Russ. Chem. Rev*., 2004, **73** (2), P. 147–159.
[36] Belyakov A.V. *Methods for Obtaining Inorganic Non–metallic Nanoparticles*. RSTU n.a. D.I. Mendeleev Publishing House, Moscow, 2003, 80 p.
[37] Zhong F., Zhao J., Shi L., Xiao Y., Cai G., Zheng Y., Long J. Alkaline-earth Metals-doped Pyrochlore $Gd_2Zr_2O_7$ as Oxygen Conductors for Improved NO_2 Sensing Performance. *Sci. Rep*., 2017, **7**, 4684.
[38] Jiang L., Wang C., Wang J., Liu F., You R., Lv S., Zeng G., Zijie Yang, He J., Liu A. Yan X., Sun P., Zheng J., Lu G. Pyrochlore Ca-doped $Gd_2Zr_2O_7$ Solid State Electrolyte Type Sensor Coupled with ZnO Sensing Electrode for Sensitive Detection of HCHO. *Sensor. Actuat. B-chem*., 2020, **309**, 127768.
[39] Sevastyanov V.G., Simonenko E.P., Simonenko N.P., Sakharov K.A., Kuznetsov N.T. Synthesis of Finely Dispersed $La_2Zr_2O_7$, $La_2Hf_2O_7$, $Gd_2Zr_2O_7$ and $Gd_2Hf_2O_7$ Oxides. *Mendeleev Commun*., 2013, **23**, P. 17–18.
[40] Tang Z., Huang Z., Qi J., Guo X., Han W., Zhou M., Penga S., Lu T. Synthesis and Characterization of $Gd_2Zr_2O_7$ Defect-fluorite Oxide Nanoparticles via a Homogeneous Precipitation-solvothermal Method. *RSC Adv*., 2017, **7**, P. 54980–54985.
[41] Liu S., Jiang K., Zhang H., Liu Y., Zhang L., Su B., Liu Y. Nano-nano Composite Powders of Lanthanum-gadolinium Zirconate and Gadolinia-stabilized Zirconia Prepared by Spray Pyrolysis. *Surf. Coat. Technol*., 2013, **232**, P. 419–424.
[42] Wei X., Back C., Izhvanov O., Khasanov O.L., Haines C.D., Olevsky E.A. Spark Plasma Sintering of Commercial Zirconium Carbide Powders: Densification Behavior and Mechanical Properties. *Materials*., 2015, **8** (9), P. 6043–6061.
[43] Yurlova M.S., Demenyuk V.D., Lebedeva L.Y., Dudina D.V., Grigoryev E.G., Olevsky E.A. Electric Pulse Consolidation: An Alternative to Spark Plasma Sintering. *J. Mater. Sci*., 2014, **49**, P. 952–985.
[44] Maslennikov D.V., Matvienko A.A., Sidelnikov A.A., Dudina D.V., Esikov M.A., Belosludov R.V., Kato H. Effect of the Synthesis Conditions of $Ce_{0.9}Gd_{0.1}O_{1.95}$ Powder on its Morphology and Characteristics of the Oxygen Ion-conducting Ceramics Obtained by Spark Plasma Sintering. *Ceram. Int*., 2021, **47** (2), P. 2557–2564.
[45] Papynov E.K., Shichalin O.O., Mayorov V.Yu., Tkachenko I.A., Golub A.V., Tananaev I.G., Avramenko V.A. Spark Plasma Sintering as Prospective Solution for Fabrication of the Functional Nanostructured Ceramics. *FEB RAS Bull*., 2016, **6** (190), P. 15–30.
[46] Sorokin O.Yu., Solntsev S.S., Evdokimov S.A., Osin I.V. Hybrid Spark Plasma Sintering Method: Principle, Posiibilities, Future Prospects. *AMIT*, 2014, **S6**, P. 11–16.

[47] Kalinkin A.M., Vinogradov V.Yu., Kalinkina E.V., Nevedomskii V.N. Preparation of nanocrystalline $Gd_2Zr_2O_7$ from mechanically activated coprecipitated precursor. *Chem. Pap*., 2020, **74**, P. 1161–1170.

[48] Terlan B., Levin A.A., Börrnert F., Simon F., Oschatz M., Schmidt M., Cardoso-Gil R., Lorenz T., Baburin I.A., Joswig J.-O., Eychmüller A. Effect of Surface Properties on the Microstructure, Thermal, and Colloidal Stability of VB_2 Nanoparticles. *Chem. Mater.*, 2015, **27**, P. 5106–5115.

[49] Terlan B., Levin A.A., Börrnert F., Zeisner J., Kataev V., Schmidt M., Eychmüller A. A Size-Dependent Analysis of the Structural, Surface, Colloidal, and Thermal Properties of $Ti_{1--x}B_2$ ($x = 0.03$–0.08) Nanoparticles. *Eur. J. Inorg. Chem.*, 2016, **6**, P. 3460–3468.

[50] Klee W.E., Weitz G. Infrared spectra of ordered and disordered pyrochlore-type compounds in the series $RE_2Ti_2O_7$, $RE_2Zr_2O_7$ and $RE_2Hf_2O_7$. *J. Inorg. Nucl. Chem*., 1969, **31** (8), P. 2367–2372.

[51] Sanjay Kumar N.R., Chandra Shekar N.V., Sahu P.C. Pressure Induced Structural Transformation of Pyrochlore $Gd_2Zr_2O_7$. *Solid State Commun*., 2008, **147** (9–10), P. 357–359.

[52] Oliver W.C., Pharr G.M. Measurement of Hardness and Elastic Modulus by Instrumented Indentation: Advances in Understanding and Refinements to Methodology. *J. Mater. Res*., 2004, **19** (1), P. 3–20.

[53] Useinov A.S. A Nanoindentation Method for Measuring the Young Modulus of Superhard Materials Using a NanoScan Scanning Probe. *Instrum. Exp. Tech*., 2004, **47** (1),P. 119–123.

[54] Maslenikov I.I., Reshetov V.N., Useinov A.S. Mapping the Elastic Modulus of a Surface with a NanoScan 3D Scanning Microscope. *Instrum. Exp. Tech.*, 2015, **58**, 711.

[55] Malygin G.A Plasticity and Strength of Micro- and Nanocrystalline Materials. *Phys. Solid State*., 2007, **49** (6), P. 1013–1033.

[56] Huang Z., Cao Z., Shi K., Qi J., Zhou M., Tang Z., Han W., Diao X., Tang J., Lu T. Synthesis and Densification of $Gd_2Zr_2O_7$ Nanograin Ceramics Prepared by Field Assisted Sintering Technique. *J. Nucl. Mater*., 2017, **495**, P. 164–171.

[57] Tuncer R., Karabaş M., Gökçe H., Kayali Y. Effect of Yb, Fe and Mo, Ti Co-doping on Thermal and Mechanical Properties of $Gd_2Zr_2O_7$ ceramics. *Ceram. Int*., 2025, **51** (19), P. 28678–28688.

[58] Zhao M., Ren X., Pan W. Mechanical and Thermal Properties of Simultaneously Substituted Pyrochlore Compounds $(Ca_2Nb_2O_7)_x(Gd_2Zr_2O_7)_{1-x}$. *J. Eur. Ceram. Soc*., 2015, **35** (3), P. 1055–1061.

Submitted 18 July 2025; revised 11 November 2025; accepted 4 March 2026

Information about the authors:

Vladimir Yu. Vinogradov – Tananaev Institute of Chemistry and Technology of Rare Elements and Mineral Raw Materials of the Kola Science Centre of the Russian Academy of Sciences, Akademgorodok, 26a, Apatity, 184209, Russia; ORCID 0000–0002–3335–5778; v.vinogradov@ksc.ru

Dina V. Dudina – Lavrentyev Institute of Hydrodynamics of the Siberian Branch of the Russian Academy of Sciences, Academician Lavrentyev Av., 15, Novosibirsk, 630090, Russia; ORCID 0000–0003–0010–4638; ddudina@hydro.nsc.ru

Maksim A. Esikov – Lavrentyev Institute of Hydrodynamics of the Siberian Branch of the Russian Academy of Sciences, Academician Lavrentyev Av., 15, Novosibirsk, 630090, Russia; ORCID 0000–0002–4845–148X; esmax@ya.ru

Olga B. Shcherbina – Tananaev Institute of Chemistry and Technology of Rare Elements and Mineral Raw Materials of the Kola Science Centre of the Russian Academy of Sciences, Akademgorodok, 26a, Apatity, 184209, Russia; ORCID 0000–0001–9591–0274; o.shcherbina@ksc.ru

Vadim V. Efremov – Institute of North Industrial Ecology Problems of the Kola Science Centre of the Russian Academy of Sciences, Akademgorodok, 14a, Apatity, 184209, Russia; ORCID 0000–0003–2407–7304; v.efremov@ksc.ru

Alexander M. Kalinkin – Tananaev Institute of Chemistry and Technology of Rare Elements and Mineral Raw Materials of the Kola Science Centre of the Russian Academy of Sciences, Akademgorodok, 26a, Apatity, 184209, Russia; ORCID 0000–0002–3668–8578; a.kalinkin@ksc.ru

Conflict of interest: the authors declare no conflict of interest.